International Journal of Ophthalmic Research

Online Submissions: http://www.ghrnet.org/index./ijor/
doi:10.17554/j.issn.2409-5680.2015.01.17

Int. J. Ophthalmic Res 2015 September 1(2): 48-58
ISSN 2409-5680

ORIGINAL ARTICLE

Novel, Noninvasive Multispectral Snapshot Imaging System to Measure and Map the Distribution of Human Retinal Vessel and Tissue Hemoglobin Oxygen Saturation

Kim Alexis Firn, Bahram Khoobehi

Kim Alexis Firn, Tulane University, 6823 St. Charles Ave., New Orleans, LA 70118, USA
Bahram Khoobehi, Louisiana State University Health Sciences Center, 2020 Gravier St., New Orleans, LA 70112, USA
Correspondence to: Bahram Khoobehi, PhD, Louisiana State University Health Sciences Center, 2020 Gravier St., New Orleans, LA 70112, USA
Email: bkhoob@lsuhsc.edu
Telephone: +1-504-568-2385 Fax: +1-504-568-2666
Received: June 5, 2015 Revised: July 26, 2015
Accepted: August 1, 2015
Published online: September 3, 2015

ABSTRACT

AIM: To design and implement a snapshot imaging system capable of mapping oxygen saturation of retinal vessels and tissue clinically for the first time.

MATERIALS AND METHODS: Our image-splitting design is attached to the imaging portions of a fundus camera. A relay subsystem and reimaging system convert reflected white light from the eye into seven monochromatic images simultaneously. Our algorithm uses intensity information at each of these discrete wavelengths to approximate the area between the oxy- and deoxyhemoglobin spectral curves, which has been shown to be proportional to oxygen saturation. We used MATLAB to convert this information into color-coded oxygen saturation maps of the optic nerve head. We validated our system by using it on a model eye with a capillary of known blood oxygen saturation, then used it *In vivo* to obtain quantitative values of human oxygen saturation for veins and tissue.

RESULTS: By collecting seven images simultaneously with one snapshot, our system is the first to document and reproducibly map oxygen saturation of the retinal vessels and tissue. Oxygen saturation values are color-coded, with oxygen-rich arteries in red, oxygen-poor veins in blue, and intermediate tissue yellow-green. Our system's calculations agree with co-oximeter readings of blood in a model eye capillary mimicking a vessel. The quantitative calculations from the healthy subject, as well as the qualitative oxygen saturation maps, show oxygen saturation levels consistent with those in the literature.

CONCLUSION: This system is clinically valuable for diagnosing and monitoring diseases affecting ocular oxygen saturation, such as glaucoma, diabetic retinopathy, age-related macular degeneration, and others. Our reliable method is capable of documenting tissue oxygenation throughout disease progression.

Key words: Multispectral; Oxygen Saturation; Snapshot; Noninvasive; Hemoglobin; Retina

Firn KA, Khoobehi B. Novel, Noninvasive Multispectral Snapshot Imaging System to Measure and Map the Distribution of Human Retinal Vessel and Tissue Hemoglobin Oxygen Saturation. *International Journal of Ophthalmic Research* 2015; 1(2): 48-58 Available from: URL: http://www.ghrnet.org/index.php/ijor/article/view/1238

INTRODUCTION

Pathologic conditions in the retina and optic nerve head (ONH) can cause vision loss and blindness. Both structures have a high demand for oxygen, and loss of the normal oxygen supply through vascular insufficiency is believed to play an important role in diseases affecting the retina and ONH. Hypoxia of the retina and ONH is believed to be a factor in the development of ocular vascular disorders, such as diabetic retinopathy (DR), arteriovenous occlusion, and glaucoma. The ability to obtain relative measurements of oxygen saturation in the human ocular fundus could aid in the diagnosis and monitoring of these and other disorders. For example, measurement of changes in retinal and ONH oxygen saturation under controlled conditions could establish relationships among oxygen consumption,

blood sugar levels, and vascular autoregulatory function in DR. Moreover, the assessment of oxygenation in the ONH may facilitate early detection of the onset of glaucoma, a disease in which timely diagnosis is crucial for effective treatment.

Collection of information about oxygenation levels in the visual system has been previously carried out with various methods, including physically invasive measurements of oxygen tension (PO2) in the optic nerve head (ONH) using O2-sensitive microelectrodes inserted into the eye[1-5]. This method allows relatively accurate determination of PO2 determination in three dimensions, but its invasive nature limits it to animal models and precludes human clinical application. Injection of a phosphorescent dye has also been used to study PO2 in the retinal and choroidal vessels, as well as the microvasculature of the ONH rim[5-7]. However, this technique has not been approved for use in humans yet. A non-invasive spectral imaging method shows promise for human clinical use. This can be a powerful tool for identifying retinal hypoxia associated with established stages of ocular disease, such as DR. Current research also seeks to document the oxygenation trend with increasingly severe glaucoma. Spectral imaging studies of retinal disorders indicate interest in developing oximetry methodology.

Khoobehi[8] and Beach[9] have previously adapted non-invasive hyperspectral imaging, which is an advanced type of spectral imaging, for recording oxygen saturation data from the primate retina. This technique, in conjunction with specialized algorithms to compute blood oxygen saturation values, was able to map relative values of saturation over the retina and optic disc. The technique was then employed in a study to determine saturation responses to elevated intraocular pressure (IOP) and oxygen breathing in a primate model for glaucoma. Results obtained by this method showed that even subtle changes in the saturation response were detected as IOP was raised. Images were acquired with a fundus camera (TRC-50vt; Topcon, Tokyo, Japan) that has a lens and a c-mount through the vertical path of the camera. An imaging spectrograph and a digital camera were used to obtain hyperspectral images. Khoobehi[8] used images with 512 spatial points and 256 spectral bands for sufficient light sensitivity and spectral resolution to monitor oxygen-dependent spectral changes in vessels. Each frame of the resulting data cube contains the spatial (x) and spectral (λ) axes for each line of the image. Successive lines form the z-axis in the stack of frames. Rotating the stack of images, by interchanging the z and λ axes, gives the "band-sequential" hyperspectral image cube. Each frame then contains a two-dimensional spatial image at a discrete wavelength.

Scanning the intensity profile along the z-axis of selected image pixels produced spectral curves for areas corresponding to arteries, veins, and tissue. These spectral curves are used to map relative oxygen saturation and produce relative saturation indices, but the scanning nature of the system requires several seconds to collect the necessary data. The typical duration of involuntary saccades is about 100 milliseconds or shorter and depends on the frequency of eye movement. Further, during the several seconds it takes to scan the eye, lighting conditions may change and unpredictably complicate the process of acquiring image data. Therefore, as a result of the sequential nature of the hyperspectral image collection, the eye must be immobilized for the duration of the imaging scan. This impedes the imaging procedure and often requires implementation of special means to prevent the cornea from drying. Although we successfully recorded oxygen saturation from immobilized retinae in anesthetized animal studies, our hyperspectral method is not rapid enough for use in a human clinical setting.

Conventionally-implemented multispectral imaging requires reconstruction of the final image from the individually obtained spectral images into a spectral data cube, or composite image, every portion of which contains the spectral information about the object. This technique involves tunable spectral filtering[11] or Fourier transform spectrometry[12]. Spectral and spatial multiplexing has low optical throughput[13]. Further, it is only applicable to temporally static phenomena.

In vivo biomedical imaging of the retina requires snapshot or time-resolved operation and high optical sensitivity[10]. Bulk-optic[14] and fiber-optic[15] high spectral resolution snapshot imaging systems require rearranging a two-dimensional image into a one-dimensional array before being converted to a spectral data cube by the computed tomographic imaging spectrometer. The one-dimensional image input is spectrally dispersed at the detector by the diffractive optical element. The data cube is formed when computer algorithms invert this data[16,17]. Image-plane spatio-spectral coding is required to recover the image[18]. Inversion is often accompanied by noise amplification, a drawback of this type of system.

A system is needed to overcome the temporal barrier to human clinical tissue oxygenation analysis posed by scanning systems without the use of injections and to avoid the inherent complications of bulk-optic and fiber-optic systems. Therefore, the dual-wavelength snapshot imaging system was developed and used by the groups of Beach, Hammer, Hardarson, and Tiedman[19-24]. They used red and green wavelengths for oxygen-sensitive and insensitive monochromatic images. They succeeded in splitting the reflected light to record pairs of retinal images side by side on a digital camera or on two different cameras simultaneously. The green wavelength was set where the oxy- and deoxyhemoglobin curves crossed with equal and opposite slopes, which kept the reference image insensitive to oxygen saturation. The red wavelength was set near the maximum of the oxy-deoxyhemoglobin difference spectrum for high sensitivity. This technique is capable of human clinical use. Our group has used this technique successfully to document oxygen saturation of arteries and veins in DR[25]. The high spatial resolution of this system, which can image the entire eye, comes at the expense of low spectral resolution. Due to having information at only two wavelengths, this system is not capable of documenting oxygen saturation of the tissue. The area between the curves of oxy- and deoxyhemoglobin obtained in hyperspectral scanning systems is proportional to oxygen saturation of tissue.

Schweitzer and Hammer's groups at the University of Jena (Jena, Thuringia, Germany) have developed systems that obtain one line of a hyperspectral image, and reported retinal oxygen saturation[26,27]. This Jena imaging spectrograph obtained optical properties from the tissue environment of the retinal vessel and fundus background[28,29]. A method of tissue analysis that can map the entire ONH with a single snapshot is needed since this method can only measure tissue oxygenation for a single line, and the hyperspectral systems can measure the tissue oxygenation for the entire ONH only in anesthetized subjects.

Once these drawbacks are addressed, spectral imaging could be a powerful tool for identifying retinal hypoxia that is associated with established stages of DR, glaucoma, central or branch vein occlusion, and age-related macular degeneration if it were quick enough to be applied clinically. For this reason, we have now developed a prototype multispectral imaging system fast enough for clinical application, using a more straightforward approach. The algorithm used to measure oxygen saturation from these seven images is deduced from the whole reflected spectrum, which we learned from animal studies using the slow system. Our non-invasive snapshot imaging system is based

on seven-wavelength oximetry. This optical instrument is capable of mapping oxygen saturation of the retinal vessels and tissue in the entire ONH by recording seven monochromatic images simultaneously onto a large chip with high dynamic sensitive digital cameras, integrated with a single optical connection to a fundus camera. Our oxygen saturation algorithm is applied to the information from these seven images to calculate oxygen saturation of retinal vessels and tissue and create entire ONH maps clinically for the first time.

This paper reviews our efforts to develop this snapshot imaging system. We will describe our multispectral imaging system and oxygen saturation algorithm. This imaging system is capable of separating the white light reflected from the retina into seven discrete wavelengths. The seven monochromatic images created from separating this scattered light are analyzed for light intensity, an indicator of the hemoglobin light absorption in the ocular structure being analyzed. The light absorbance of a certain structure in the eye, such as a vessel or tissue area, at each of these seven wavelengths is directly proportional to the relative hemoglobin oxygen saturation. Our algorithm has been coded into a MATLAB program capable of transforming images into color-coded oxygen saturation maps of the eye. We validate this imaging system by applying it to a model eye with blood of known oxygen saturation. Then, we report our preliminary quantitative human results for a healthy subject.

METHODS

Multispectral Imaging Instrumentation Design

We designed and created a snapshot multispectral imaging system. The system can obtain seven monochromatic images simultaneously. The prototype capable of splitting images is attached to the imaging portions of a commercially available fundus camera (Zeiss FF450 IR). Traditionally, a patient's eye image is captured through a fundus camera at the pupil (A).

The schematic of the attachment to the fundus camera is shown in Figure 1, which includes a relay subsystem and has an entrance pupil (B). The entrance pupil (B) is the same as the exit pupil (A) of the fundus camera. A reimaging subsystem (RI) includes a bandpass filter array (D) and an array of secondary objectives (E), which is positioned at an exit pupil (F) of the relay subsystem. Each of the individual objectives of the array (E) focuses light on a 2-D focal plane detector to produce individual spectral images of the retina of the eye. In this particular device, we made a prototype of a reimaging subsystem (RI) with seven lenses and bandpass filters.

In reference to Figure 1, the five elements (lenses) of the relay subsystem can be divided into three groups. The first (positive) group with the primary objective 1, the second (correction) group with lenses 2, 3, and 4, and a third (positive) group with lens 5. The first and third groups operate to reimage and expand the exit pupil (B) of the fundus imaging device into the exit pupil (F) of the relay subsystem (RI). The second group is configured to correct optical aberrations that would otherwise render the optical quality of the images unusable. An image frame containing individual spectral images is further developed with a computer processor and appropriate data processing algorithms to produce a resulting aggregate multispectral image frame.

Figure 2 shows detail of the RI and the images formed. The transverse dimensions of the exit pupil (F) are preferably slightly larger than those of the RI to avoid vignetting and/or shadowing effects. There are seven different bandpass filters that have been used (3 oxygen-sensitive at 542, 560, and 577 nm; 4 isosbestic at 522, 548, 569, and 586 nm). As shown in Figure 3, each of the individual

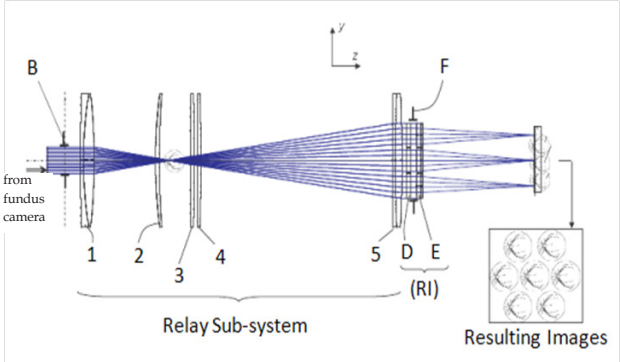

Figure 1 A schematic of the beam-splitting attachment to the fundus camera. The relay sub-system in this figure consists of five different lenses (1-5). These can be divided into three groups: a first positive group with primary objective (1), a second correction group with the lenses 2, 3, and 4, and a third positive group with lens 5. The first and third groups operate to reimage and expand the exit pupil (B) of the fundus imaging device into the exit pupil of the relay sub-system. The second, correction group (lenses 2, 3, and 4) is configured to correct optical aberration that would otherwise render the optical quality of the images unusable. An entrance pupil (B) for the imaging system is the same as the exit pupil for the fundus camera. The transverse (with respect to an optical axis) dimensions of the exit pupil (F) are preferably slightly larger than those of the reimaging sub-system to avoid vignetting and/or shadowing effects. The reimaging sub-system includes a bandpass filter array and an array of secondary objectives, which are positioned at an exit pupil of the relay sub-system. Each of the individual objectives of the array focuses the light on a 2D focal plane detector to produce individual spectral images of the retina. The individual images are further shown in an image frame (Resulting Images).

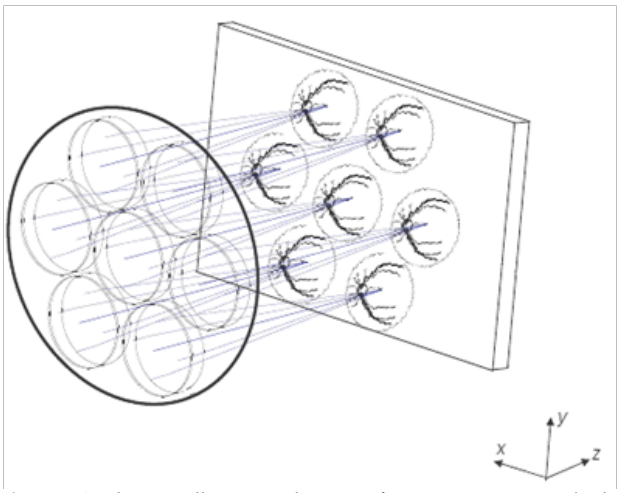

Figure 2 A schematic illustrating the image frame containing a multiple of individual images, each of which retains spectral responses of the corresponding bandpass filters.

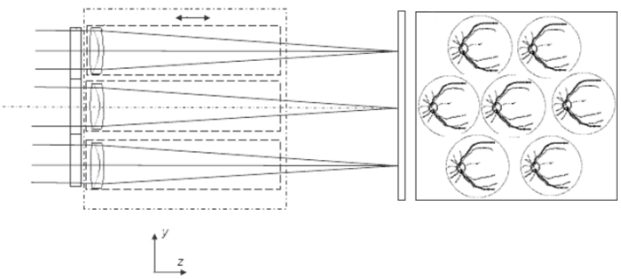

Figure 3 A collection of individual secondary objective lenses of the reimaging sub-system that are repositionable via an associated elongated lens barrel providing a means for readjusting the position of the given secondary objective lenses.

secondary objective lenses of the RI is individually repositionable via an associated elongated lens barrel. This provides a means for readjusting the positioning of the given secondary objective lenses along the optical axis to obtain a highly focused corresponding individual image frame. The lens barrels are assembled in a single mount that utilizes a barrel-locking mechanism to maintain the position of the lens barrels after the focus adjustment. We used this snapshot system to image the fundus. The outcome is seven identical monochromatic images recorded in a 32 MB chip with 16 bit high dynamic resolution.

We designed a more compact layout without changing the optical path of the overall system, shown in Figure 4. This configuration makes the system compact and facilitates its integration with the fundus camera. In Figure 4, the lenses are labeled in the same fashion as in Figure 1. Several adjustable folding mirrors are utilized (labeled M in Figure 4) and lens 3 of the relay subsystem is removed to accommodate the preferred optical layout. Array D contains seven optical filters with corresponding bandwidths of about 4 nm centered at 522 nm, 542 nm, 548 nm, 560 nm, 569 nm, 577 nm, and 586 nm, respectively. The image frame contains seven individual images retaining individual spectral responses of corresponding individual bandpass filters. This frame is further split into individual images that are processed and recombined, with the use of a computer processor, into a final composite multispectral image.

Optical design parameters for this snapshot multispectral imaging system are summarized in figures 4 through 8. Figure 4 illustrates the geometrical layout of the imaging system, while Figure 8 presents transmission characteristics of the optical filters of the array D. Figures 6 and 7 illustrate spot diagrams associated with an imaging system having a full aperture and that of the imaging system with a segmented aperture, respectively. As expected, the diffraction limit of the resulting image of the segmented aperture system is slightly lower than that of a full-aperture system where the exit pupil of the relay sub-system is not spatially segmented. These diffraction limits are 12.21 microns and 3.66 microns, respectively. Calculations are obtained from an optical software design program (Zemax) and are shown in Figure 5. Reduction in spatial resolution does not affect this system's use in ophthalmologic imaging, where the spatial resolution of the eye remains a limiting factor.

A typical set of seven monochromatic images of a human fundus obtained from the system are shown in Figure 9. These images have a 16 bit original dynamic range. However, the screen limits the viewing capacity to 8 bit resolution. The resulting images are arranged from 522 nm at 11:00 to 577 nm at 1:00 in a counterclockwise fashion with the 586 nm image in the center.

Algorithm

A hyperspectral algorithm was developed in our laboratory for the quantification of oxygen saturation in retinal artery and ONH tissue[8,9]. Figure 10 shows the whole spectrum for oxy- and deoxyhemoglobin obtained from reflected artery and vein overlaying the ONH[8,9]. This whole spectrum was obtained from the ONH of a nonhuman primate. The reflectance oxyhemoglobin spectra in this figure was achieved by letting the animal breathe pure oxygen. The reflectance deoxyhemoglobin spectra was obtained from desaturating oxyhemoglobin by applying a suction cup to the eye and raising IOP to 45 mmHg. At this high IOP, perfusion stops at the fundus for a short period of time and blood and tissue become desaturated[8,9]. Animals had to be anesthetized to immobilize the eye, which was held open for the duration of an imaging session. Any involuntary eye movement that might occur in the conscious animal would compromise the data.

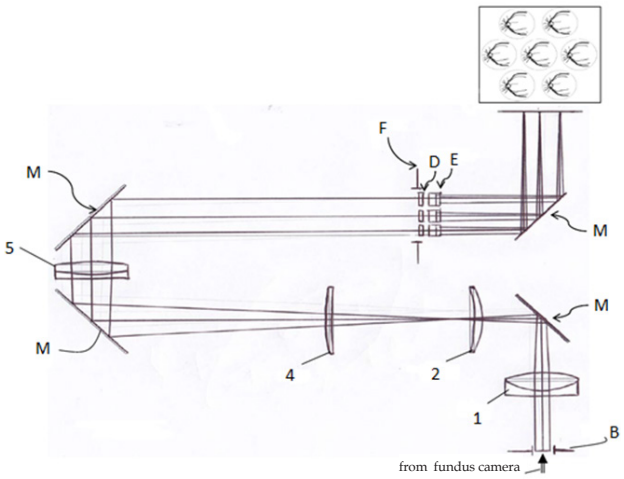

Figure 4 A schematic of the imaging system attached to the fundus camera, detailing image formation. This layout is specifically adapted to make the system more compact. This facilitates integration of the attachment to the fundus camera. In the figure, M are the mirrors. D is the array containing seven optical filters having corresponding bandwidth of 4 nm centered at 522, 542, 548, 560, 569, 577, and 586 nm. B and F are the entrance and exit pupils, respectively, of the attached system. 1, 2, 4, and 5 are lenses. E is an array of lenses.

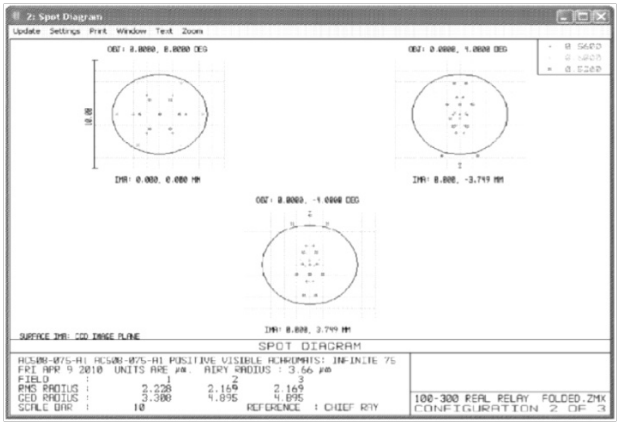

Figure 6 A spot diagram of an optical system of Figure 4 without segmentation of light at the exit pupil of the relay subsystem with an array of optical lenses.

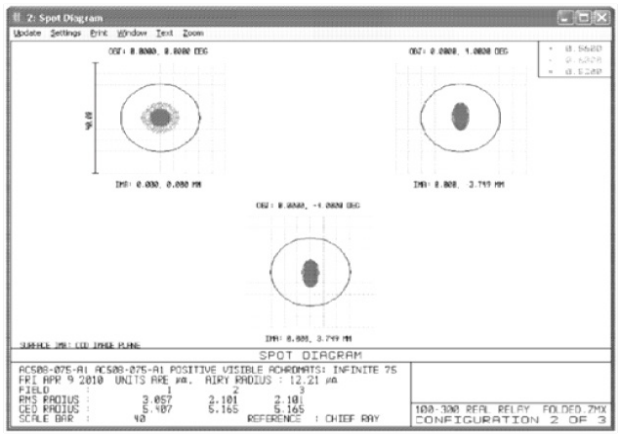

Figure 7 A spot diagram corresponding to the output of Figure 4, with segmentation at the exit pupil.

	Surf: Type	Comment	Radius	Thickness	Glass	Semi-Diameter
OBJ	Standard		Infinity	Infinity		Infinity
STO	Standard	Zeiss Exit Pupil…	Infinity	41.244		5 U
2*	Standard	Edmund Optics 45353	446.01	4	N-SF10	25 U
3*	Standard		46.95	13.92	N-BAF10	25 U
4*	Standard		-69.28	40		25 U
5	Coordinate B…			0		0
6*	Standard	Thorlabs P20-03-P01	Infinity	0	Mirror	25 U
7	Coordinate B…			-40.545		0
8*	Standard	JML CMN11250100	-57.74	-5	BK7	25 U
9*	Standard		-101.58	-96.722		25 U
10*	Standard	JML CMN11250100	600	-4	BK7	25 U
11*	Standard		204.95	-160		25 U
12	Coordinate B…			0		0
13*	Standard	Edmund Optics 32135	Infinity	0	Mirror	34 U
14	Coordinate B…			31.577		0
15*	Standard	Edmund Optics 45181	709.83	3.5	N-SF10	25 U
16*	Standard		164.03	9	N-BAK4	25 U
17*	Standard		-173.11	33.88		25 U
18	Coordinate B…			0		0
19*	Standard	Edmund Optics 32135	Infinity	0	Mirror	34 U
20	Coordinate B…			-230		0
21	Coordinate B…			0		0
22	Standard	Relay Exit Pupil…	Infinity	0		4.5 U
23*	Standard	Edmund Optics 32494	-91.37	-5.7	N-BK7	4.75 U
24*	Standard		66.21	-2.2	N-SF5	4.75 U
25*	Standard		197.71	7.9		4.75 U
26	Coordinate B…			-7.9		0
27	Standard		Infinity	-68.164		13.962 U
28	Coordinate B…			0		0
29*	Standard	Thorlabs P20-03-P01	Infinity	0	Mirror	25 U
30	Coordinate B…			78		0
IMA	Standard		Infinity			3.776891

Figure 5 A summary of optical design parameters of Figure 4 using an optical software design program (Zemax).

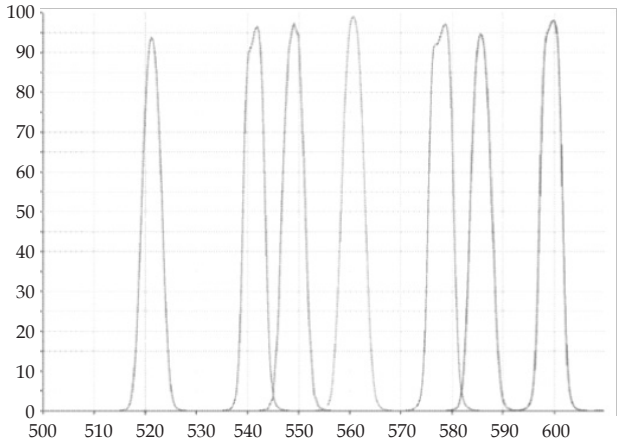

Figure 8 Transmission characteristics of the optical filters shown in Figure 4.

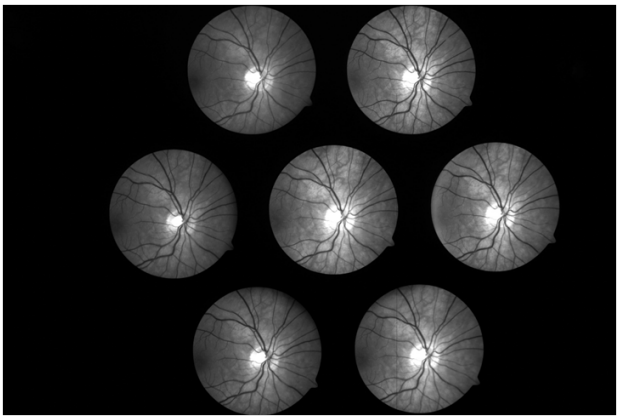

Figure 9 A typical set of seven monochromatic images produced from bandpass filters.

As seen from the figure, there are four points where the oxy- and deoxyhemoglobin spectra intersect. These four points are at oxygen-insensitive (isosbestic) wavelengths. In other words, these four points have the same absorption and reflection for oxy- and deoxyhemoglobin. Previously, we developed an algorithm that measures oxygen saturation from the whole spectrum. Briefly, we proved oxygen saturation is proportional to the areas trapped by the spectrum and the lines that connect the isosbestic points to each other. As seen in Figure 6, the whole spectrum has three minimum or maximum points, which are oxygen-sensitive. Using these three oxygen-sensitive points (542, 560, and 577 nm) and four isosbestic points (522, 548, 569, and 586 nm), we can construct three triangles which have areas proportional to oxygen saturation, as shown in figure 11. We constructed an algorithm based on these seven discrete wavelengths from the whole hemoglobin spectrum. Discrete spectral curves from individual pixels within the border of each structure can be constructed (Figure 11). These curves are then fit to a linear combination of reference curves obtained from fully saturated and desaturated red cell suspensions. Before performing the curve fit, the recorded spectrum is transformed by the method of Hammer

et al. to remove influences of nonhemoglobin light absorption and light scattering[30]. This transformation corrects the recorded curves at three isosbestic wavelengths (522, 569, and 586 nm) to match the corresponding intersections of the reference curves for oxygenated and deoxygenated blood. Saturation is measured at 560 nm, which is a maximum in the difference spectrum. We use the same procedure to test the calibration of red cell suspensions. Then we determine saturation by least square fits to oxygenated and deoxygenated reference curves from red cell suspensions.

We find the oxygen saturation obtained as described above is proportional to the summation of three triangles normalized to the intensity of the incident light. These triangles are constructed with four isosbestic and three oxygen-sensitive wavelengths.

Curve fits are performed with a Windows software package (MathGrapher 2.0; Springfield Holding b.v., Noordwijk, The Netherlands). Reference spectra of saturated (Ssat) and desaturated (Sdesat) red cell suspensions are fit to transformed retinal blood spectra (S) using fitting parameters A and B with an additive term (C), as in Eq. (1):

$$S = A \times Ssat + B \times Sdesat + C. \quad (1)$$

Percent oxygen saturation is determined by expressing fitting parameters as in Eq. (2):

$$\%Sat = 100 \times A/(A + B), \quad (2)$$

Where A and B correspond with best-fit coefficients for oxyhemoglobin and deoxyhemoglobin contributions as defined by Eq. (1).

To calibrate the system *In vivo*, we are going to use the approach used by Hammer *et al*[30] to correct for light level and tissue pigmentation.

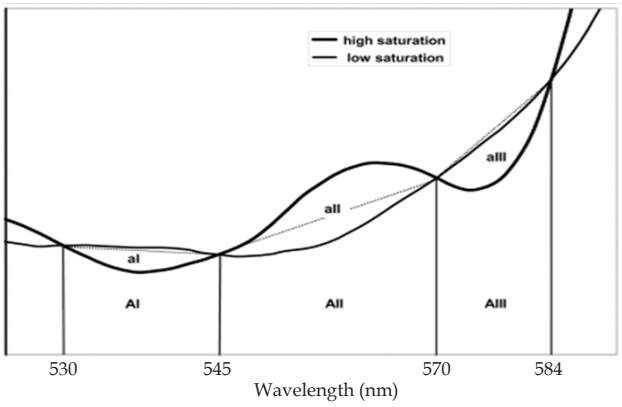

Figure 10 The whole reflectance spectra for oxy- and deoxyhemoglobin obtained from reflected artery and vein overlaying the ONH.

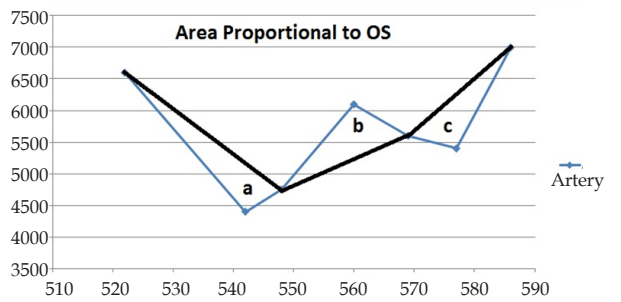

Figure 11 The whole spectra for oxy- and deoxyhemoglobin obtained from reflected artery and vein overlaying the ONH.

Hammer's method[30] uses a series of linear transformations to mitigate non-hemoglobin absorption and tissue scattering. In order for this procedure to work, reference spectra of 100 percent oxygenated blood and fully desaturated blood need to be known. The spectra are forced to have equal end points at the isosbestic wavelengths of 522 nm and 586 nm. This is done by first making a linear function connecting the start and end points of isosbestic wavelengths (522 nm and 586 nm) for the references and vessel spectrums, g(λ) and f(λ) respectively. The measured spectral curves (Mλ) are then transformed by an equation for all wavelengths to correct for light level. The next step is to force the spectra to go through the same point at 548, which is done using an equation to correct for tissue pigmentation. The final calculation involves the relative intensity of the transformed spectrum at 560 nm (oxygen-sensitive wavelength) to the reference spectrum[30]. Hammer used this technique for the whole hemoglobin spectrum. We followed the same procedure to obtain seven wavelength multi-spectral images.

In vitro study with a model eye

To validate our results, we prepared differentially oxygenated blood samples and placed them in a model eye to be imaged by our system. The model eye was designed to mimic the optics of the human eye, consisting of a 60-diopter lens and a chamber filled with circulating water. A 50-μm tube connected to a circulating pump was placed at the image plane of the lens, acting as a model retina. The differentially saturated solutions were then individually run through the tube and imaged by our multispectral imaging system.

After the plasma was removed from the blood sample, it was re-suspended in an aqueous buffer solution. We bubbled oxygen gas through the solution bringing it to complete 100 percent saturation. We then bubbled nitrogen gas through the solution for different amounts of time to get set levels of oxygen saturation. Using a co-oximeter (Instrumentation Laboratory Co-Oximeter Model 682), we measured oxygen saturation of each sample.

In vivo sample of a healthy human subject with quantitative values

This study was approved by the Institutional Review Board of LSU. It adheres to the tenets of the Declaration of Helsinki. The subjects provided informed consent before participation in the study and went through standard study protocol. After consenting to be in the study, the subjects answered a questionnaire about medical history.

The healthy subject imaged and analyzed in this study is a 54-year-old Caucasian male with olive skin pigmentation. Figure 12 shows the area where measurements were taken from the healthy subject for oxygen saturation values. As indicated, we divided the image into four concentric circles. Area 1 is located on the perimeter of the inner circle. The numbers of the areas increase radially outwards, with Area 4 being on the outermost circle. Superotemporal, superonasal, inferotemporal, and inferonasal areas of both vein and tissue were measured for each of four distances from the ONH. Those distances were (1) just outside the ONH; (2) one ONH diameter from the ONH edge; (3) two ONH diameters from the ONH edge; and (4) three ONH diameters from the ONH edge. For the vein areas, ten pixels are averaged to get the oxygen saturation reading. For the tissue areas, 80 pixels are averaged. The vein values are calculated by comparing vein intensity to artery intensity, which we set to 96 percent saturation.

Oxygen saturation maps

The seven monochromatic images from a single snapshot of our

system are used to create a color-coded oxygen saturation map of the eye. After registration of the seven monochromatic images, color-coded MatLab figures are generated by our MATLAB script, as described in previous work[8]. Spatial resolution is per pixel, but oxygen saturation values are relative. The reported number is the average of a certain amount of pixels. The oxygen saturation values are color-coded in a gradient from highest in red to lowest in blue. The arteries appear red to show high oxygen saturation. The veins appear blue to show low oxygen saturation. The tissue appears yellow-green to show intermediate oxygen saturation. We imaged a healthy 35-year-old Caucasian woman, and we show the seven simultaneously obtained monochromatic images and the oxygen saturation map for this subject in the results section. Also, different technicians imaged a healthy 38-year-old Caucasian woman on separate days to show reproducibility of our oxygen saturation maps.

RESULTS

***In vitro* study with a model eye**

We detailed the creation of a model eye with blood of known oxygen saturation run through a capillary mimicking a retinal vessel within the model eye cavity. The results from our imaging system and algorithm's use on our model eye are plotted against the known blood oxygen saturation in Figure 13. There is a linear correlation between oximeter readings and our system's calculations.

The x-axis in the figure indicates the oxygen saturation values of the blood samples that we obtained from different aliquots. The raw data was converted to oxygen saturation by our algorithm and plotted on the y-axis. The co-oximeter values vary linearly with our algorithm's values, with R^2=0.984, as shown in the figure.

***In vivo* sample of a healthy human subject with quantitative values**

Table 1 indicates average oxygen saturation values for vein regions corresponding to Areas 1 through 4, respectively. The last row in the table gives the average saturation from all radii for each region. Table 2 is the analogous chart for tissue regions. These values are obtained from our previously mentioned algorithm, with an assumption that the arteries have an oxygen saturation of 96 percent. Each region's oxygen saturation is an average of the values from day 1 and day 7 of oxygen saturation calculation.

To test reproducibility we repeated the multispectral imaging in two different sessions, seven days apart, and averaged the results. The values for the vein changed from 63 ± 4.7 percent to 59 ± 2.9 percent, and the values for the tissue changed from 71 ± 4.8 percent to 76 ± 4.5 percent. The average value taken from all vein areas was found to be 61 percent, whereas this average oxygen saturation value for the tissue was 76 percent. We found that the oxygen saturations of the superotemporal, inferotemporal, and inferonasal veins were of similar values, ranging from 62 to 63 percent. That of the superonasal vein, however, was significantly lower, at 54 percent ($p \leqslant 0.05$). We also found that all of the oxygen saturations for the tissues in different quadrants of the eye were quite similar to each other, ranging from 74 to 77 percent.

The percent oxygen saturations of the superotemporal vein, superonasal vein, and of the superotemporal tissue all tended to decrease as one moved radially farther from the ONH, toward the periphery of the image. The inferotemporal and inferonasal veins, as well as the inferotemporal, inferonasal, and superonasal tissues, did not show any correlation between distance from the ONH and percent oxygen saturation.

Oxygen saturation maps and reliability

The seven images in Figure 9 were converted to a color-coded figure of oxygen saturation, which is shown in Figure 14 for a typical ONH. Images from this system's clinical use *In vivo* show that the results are reliable and reproducible. The images, calculations, and color-coded oxygen saturation maps are relatively constant for a given patient on different days as taken by different technicians. The patient whose images are compared here had no known ocular health changes between image acquisition trials. Figure 15 shows two color-coded oxygen saturation maps of the fundus of the same patient imaged on different days by different technicians, exhibiting reliability.

DISCUSSION

Laser doppler flowmetry has shown that various retinal diseases and treatments are associated with significantly altered blood flow rates. The establishment of a relationship between altered blood flow and

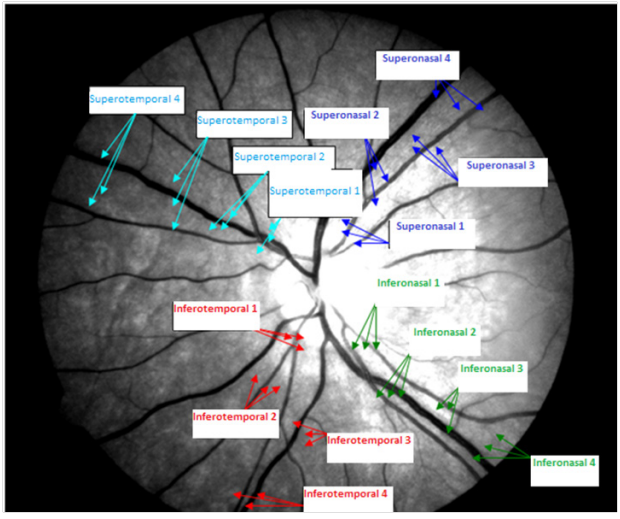

Figure 12 An image key of one of the seven monochromatic images from our system identifying areas surrounding the ONH analyzed for oxygen saturation. An area from within a vein and an area of adjacent tissue were analyzed in the area just outside the ONH (area 1), an area one ONH diameter away from the center of the ONH (area 2), an area two ONH diameters away from the center of the ONH (area 3), and an area three ONH diameters away from the center of the ONH (area 4).

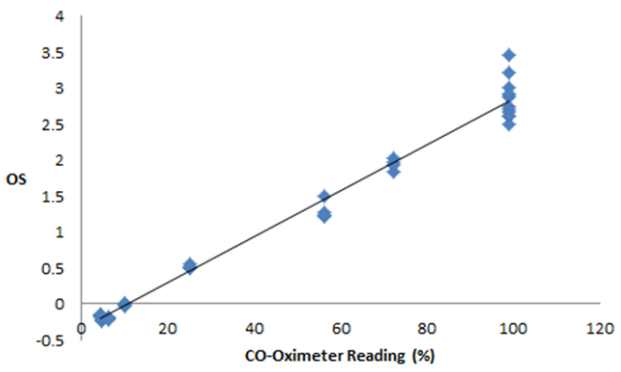

Figure 13 Plot of co-oximeter readings for blood in a model eye capillary versus oxygen saturation calculations from our system. The plot has an R^2 value of 0.984, showing good agreement between the two methods of measurement.

pathogenesis of diseases and the prospect of diagnosis based on functional changes are exciting new developments. After background retinopathy is established in diabetic individuals, adjacent areas of high and low blood perfusion are often visualized by fluorescein angiography. Areas of low perfusion become hypoxic and, over time, become sites of neovascularization which leads to proliferative retinopathy and blindness. Areas of high perfusion subject retinal capillaries to unfavorable flow and pressure over time. This stress is believed to cause the microaneurysms and hemorrhages which are first clinical signs of retinopathy. Structurally compromised retinae may receive a normal supply of oxygen. However, if inner retinal oxygen consumption is increased during periods of hyperglycemia, even these areas could experience relative hypoxia[31]. The pathogenic mechanisms leading to adjacent high and low areas of blood flow are not well understood. Possibly this situation could result from impaired blood flow autoregulation caused by high blood sugar. Regardless of the origin, a means of identifying hypoxic retinal tissue would be extremely valuable, both to identify individuals at risk for severe stages of retinopathy prior to development of structural pathology and to investigate how oxygen utilization is implicated in pathogenesis of retinopathy. An ability to detect and correct abnormal retinal function before any vascular and tissue damage can occur will greatly improve outcomes and avoid injury. The development of an instrument capable of oximetry of the ocular fundus enables such detection.

Several oximetry studies based on the dual-wavelength method of Beach *et al*[19] have been reported recently. Harris *et al*[32] evaluated the performance of dual-wavelength oximetry by imaging vessels near the optic disc. Crittin *et al*[33] reported time resolved measurements of venous saturation in response to breathing 100 percent oxygen using the dual-wavelength technique. A commercial version of the dual-wavelength imaging method was introduced by Oxymap company (Iceland) and it employed the two wavelengths used by Beach *et al*[19] earlier. This system splits retinal images into two separate wavelengths that are recorded on two separate sensors. It measures the relative optical density from oxygen-sensitive and insensitive images, and it relates the relative optical density to oxygen saturation. The system is capable of measuring oxygen saturation in the fundus vasculature, but not tissue.

Table 1 Average vein oxygen saturation values for the four areas of increasing radius from the ONH. The percent oxygen saturation was calculated by comparing the intensities to that of an arterial area, which was set to correspond to 96 percent saturation. The vein oxygen saturation values are much lower than arterial oxygen saturation.

Vein	Area 1	Area 2	Area 3	Area 4	Overall
Superotemporal	68% ± 1%	65% ± 0%	61% ± 10%	54% ± 2%	62% ± 7%
Inferotemporal	65% ± 6%	61% ± 5%	65% ± 1%	60% ± 1%	63% ± 4%
Inferonasal	66% ± 4%	60% ± 3%	66% ± 2%	61% ± 6%	63% ± 4%
Superonasal	57% ± 4%	53% ± 1%	54% ± 5%	53% ± 3%	54% ± 3%

Table 2 Average tissue oxygen saturation values for the four areas of increasing radius from the ONH. The percent oxygen saturation was calculated by comparing the intensities to that of an arterial area, which was set to correspond to 96 percent saturation. The tissue oxygen saturation values are intermediate between the vessels.

Tissue	Area 1	Area 2	Area 3	Area 4	Overall
Superotemporal	80% ± 3%	75% ±1%	73% ± 4%	74% ± 7%	77% ± 4%
Inferotemporal	76% ± 5%	77% ± 4%	76% ± 3%	73% ± 4%	76% ± 3%
Inferonasal	79% ± 5%	71% ± 1%	76% ± 1%	74% ± 1%	74% ± 2%
Superonasal	74% ± 5%	77% ± 4%	80% ± 3%	76% ± 6%	77% ± 4%

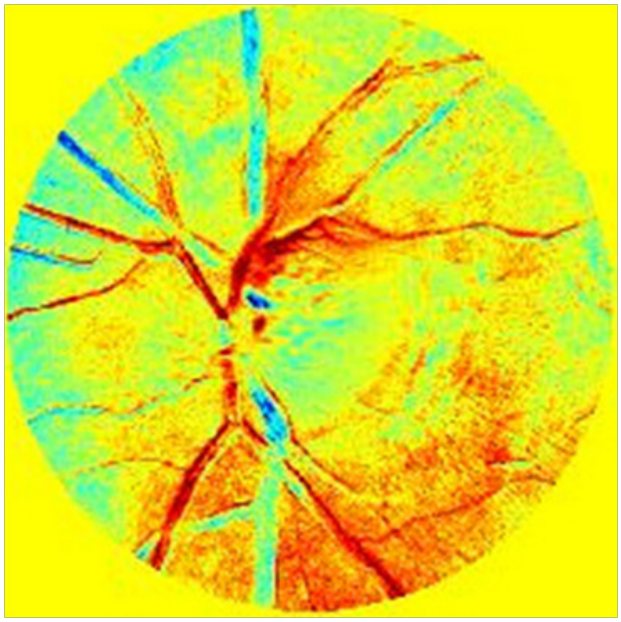

Figure 14 A color-coded oxygen saturation map from an individual with lighter pigmentation. The values are relative and reflect pixel group averages.

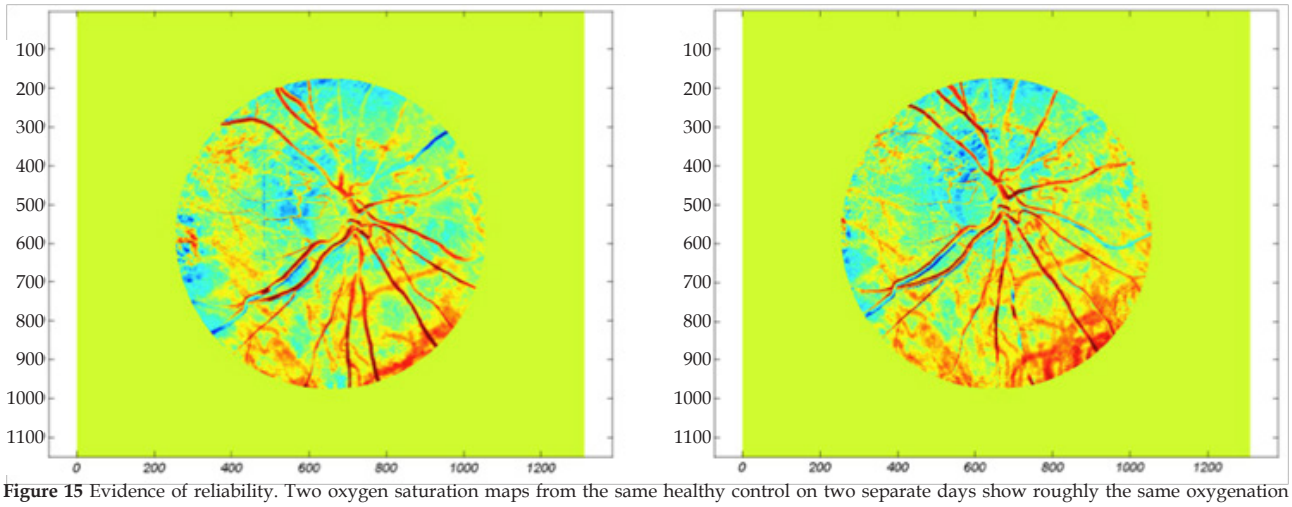

Figure 15 Evidence of reliability. Two oxygen saturation maps from the same healthy control on two separate days show roughly the same oxygenation patterns. The relative oxygen saturation is color-coded from blue (low) to red (high).

Another method combines visualization of flow and oximetric state using rapid flash sequences[34]. The hypoxic areas shown from this instrument were under areas of retinal hemorrhage and were not clear in the image; more results are needed to confirm this approach for clinical assessment.

The above techniques measure the oxygen saturation of retinal veins and arteries. We developed a snapshot method capable of taking multiple images simultaneously using seven wavelengths, determined to be necessary by hyperspectral imaging, to find the oxygen saturation not only in blood vessels but in the retinal tissue as well. Our system is the first noninvasive imaging system capable of documenting the oxygen component of both vessels and tissue clinically. Hemoglobin oxygen saturation is a biomarker that varies with severity of several prevalent conditions, such as glaucoma, DR, macular degeneration, retinopathy of prematurity, retinal artery and vein occlusion, and others. A quick, easy, affordable diagnostic and disease monitoring technique would be an extremely valuable clinical tool.

A basic spectral imaging system includes a detector or a detector array positioned in the imaging plane of an optical system that images a scene or an object, and a series of optical filters (e.g., bandpass filters defining different spectral regions of imaging) intersecting the beam of light delivered to the imaging plane. Individually obtained spectral images can be taken in a sequence (in a system having a single imaging channel) or simultaneously (in a multi-channel system). Imaging with the use of a single-channel system typically requires changing optical filters one at a time. The final image is then reconstructed from the individually obtained spectral images into what is sometimes referred to as a "spectral cube" or a "composite image," every portion of which contains the spectral information about the object. In many circumstances, the object being imaged is not stationary. This complicates imaging with a single-channel system because sequentially acquired images from one another and require complicated reconstruction processes. In other cases, such as medical imaging, it is not feasible to take many images due to patient compliance issues or limited allotted time. Our snapshot multispectral imaging technique circumvents these shortcomings by obtaining seven images simultaneously.

The aperture stop of an optical system is the location where the rays from every point of a scene cross. It is typically where a fixed or adjustable iris is positioned to control the amount of light going through the optical system. Its size determines the f-number of the optical system. The pupil of an optical system is the image of the aperture stop as seen by the object (entrance pupil) or by the image (exit pupil). As in the case of the aperture stop, the exit pupil is where the rays originating from a point of the object cross everywhere in the pupil. This unique feature enables the pupil to be segmented into smaller portions, each containing all the spatial information from the object. In order to construct a multispectral imaging system, a series of objective lenses are arranged in the exit pupil in a hexagonal pattern with a seventh lens in the center. Each lens produces an individual image of the scene on the focal plane. The focal length and diameter of the individual objective lenses determine the size and spacing of the scene image on the focal plane. Those parameters are adjusted to optimally fill the focal plane and obtain the highest spatial resolution. In addition, the objective lenses are preceded by a filter, each covering a specific wavelength of interest. The final multispectral image is reconstructed using the individual images contained in the single file.

Our new idea arises from the realization that the use of a two-dimensional array of secondary objective lenses positioned to spatially split or segment the incoming beam at the image plane of the entrance pupil significantly simplifies the multispectral, multi-channel imaging system. In such a configuration, the array of secondary objectives performs the beam-splitting role, and there is no need for a separate beam-splitting component. As a result, folding of the optical path can be avoided. Additional advantages of this configuration include simplicity of assembly, modularity, and reconfigurability of the imaging system.

In conventional multi-channel systems, precision and symmetry of the positioning of beam-splitting components in a transverse (with respect to the optical axis of the system) plane defines the resulting spatial resolution in the image plane. However, in applications that do not require imaging systems with maximized spatial resolution or that can employ imaging systems having spatial resolution below a pre-defined threshold, axially-asymmetric positioning of the secondary objectives forming multiple images in the imaging plane can be sufficient. Using secondary objectives of the reimaging subsystem at the exit pupil to spatially segment the incoming beam allows us to avoid the use of auxiliary beam-splitting components used in previous imaging techniques[14]. This increases the system tolerance to mechanical misalignments.

Another advantage of our imaging system is the ability to record a complete spectral image using a two-dimensional focal plane detector array in a single exposure, without the need for spatially deviating the image-forming beams from one another. This greatly helps in the recombination of the individual images into a single spectral image. This advantage is particularly pronounced in applications involving imaging of dynamic objects, such as the eye of a conscious animal.

We built a system capable of retinal oximetry and we validated it using a model eye. Our *In vitro* study shows a linear correlation between co-oximeter readings and our multispectral method with R^2=0.984. The red blood cell suspension in our *In vitro* study is free of any tissue pigmentation. Adjusted curves (seven reflectance intensity values at discrete wavelengths connected to each other) from red cells with different levels of oxygenation and from deoxygenated red cells are plotted with curves obtained from retinal arteries of a normal subject. Then, saturation of all samples were determined at a wavelength of 560 nm by the method of Hammer[20]. For the oxygenated red cells with 96 percent oxygenation read by the co-oximeter, our method agrees within 2 percent of the 96 percent reading.

We draw four major conclusions from these experiments with our technique. First, the venous oxygen saturation values are reproducible, since they are comparable to other investigators' data. However, our superonasal vein results are lower than our other vein results, which does not agree with other studies. With an increased study sample, this effect will likely disappear. Since this is a feasibility study for proof of concept, we only evaluated one eye. A dual-wavelength study by Geirsdottir *et al*[35] found the inferotemporal quadrant to have lower oxygen saturation measurements than other quadrants for both arterioles and venules. Retinal oxygen saturation is individually variable, and our subject's results shows variation from the results of Geirsdottir's group. On the whole, our data from veins demonstrate that we are recording results very similar to other human trials[19,36-37]. Hammer and Schweitzer *et al* found in their study[36] that the mean venous oxygen saturation was 65±11.7 percent, which our data corroborates. Stefansson and coworkers[37] found in their research that the percent oxygen saturation in retinal veins was 63±5 percent, substantiating our range of values. Also confirming our results were Beach *et al* who found that the percent oxygen saturation of retinal veins in subjects breathing room air ranged from 54 percent

to 62 percent[19]. Confirming our venous values with other techniques indicates that our spectrum technique leads to similar results as those obtained by the optical density approach used by others[19,36-37].

In future studies, we will calibrate our system to standardize the results with those from the accepted dual-wavelength method. This will prevent having to assume arterial saturation is always 96 percent, and allow us to measure differences in arterial saturation, as well. Our system requires an arterial reference oxygenation because we did not calibrate our results with an accepted system, such as the dual-wavelength method. Alternatively, we could have altered oxygenation externally through oxygen-breathing and monitored percent oxygen saturation corresponding to our readings, but we have not done this. If the actual arterial saturation is lower or higher than 96 percent, the vein and tissue values will appear too low or too high, respectively. We did not apply our algorithm's values from the model eye study to our in vivo system because the model eye pipette is not in the same environment as a real vessel. Therefore, the resulting values are not corrected for real conditions, like pigmentation. The in vitro model eye study only confirmed our algorithm gives a linear relationship with spectrometer readings.

Second, our technique is the first non-invasive imaging method capable of measuring oxygen saturation of microcirculation, or retinal tissue. The oxygen saturation values that we measured for the retinal tissue include the signal generated by the choroid, as well. These two tissues cannot be separated by this technique. However, we speculate that the signal generated by the choroid is not significant in this particular subject. The subject had olive skin pigmentation and the color fundus image shows dark retinal pigment epithelium. Therefore, the signal generated from the choroid is minimal. This conclusion is supported by our results, which show that all four areas radiating outward from the ONH edge are similar. The area just outside the ONH is composed of the nerve fiber layer, or the fibers converging to form the optic nerve. This area is much like the actual ONH in that it does not have a background contribution from the choroid. If all areas show similar oxygenation results, and if area 1 has the same background as the ONH, then it appears that there is no difference in background signal affecting our oxygenation results. If areas 2, 3, and 4 had a significant choroidal contribution, they would all vary from area 1 due to this effect. The superotemporal tissue region does show a decreasing trend moving radially outward from the ONH, but if this were due to choroidal contribution, all regions would show this trend.

Third, our system is able to map oxygen saturation throughout the entire retina. The current study is the first to our knowledge to report and map the distribution of blood oxygen saturation in retinal structures. There was good agreement between qualitative results obtained by the mapping method algorithm developed by our group and our quantitative oxygen saturation results. Both the quantitative results from a healthy subject in Tables 1 and 2 and the qualitative results from two different healthy subjects in Figures 14 and 15 showed that the order of high, intermediate, and low saturation in, respectively, the retinal arteries, retinal tissues, and retinal veins, are as expected. The advantage of averaging intensity values from pixels in areas of interest, as was done to generate the oxygen saturation values for veins and tissue areas in Tables 1 and 2, is noise reduction. Significant additive noise appears on multispectral curves from single pixels. Figures 14 and 15 are generated from such single pixel recordings and exhibit increased noise.

Fourth, our results are reliable. As previously mentioned, the quantitative values obtained from the healthy subject on days 1 and 7 for each region (superotemporal, superonasal, inferotemporal, or inferonasal) and area (1, 2, 3, or 4) do not vary significantly. Further, the color-coded oxygen saturation figures mapping the oxygenation of the eye are reliable, as shown by Figure 15. These methods for generating oxygen saturation percentages and relative values for color-coded maps are invaluable clinical tools, and these results confirm that our method is reliable.

In conclusion, our reliable method for clinical documentation and mapping of vessel and tissue oxygen levels is novel and of clinical relevance. Our system overcomes the inherent drawbacks of previous oximetry methods, and can be used to monitor disease state noninvasively.

ACKNOWLEDGMENTS

We would like to acknowledge the support of Louisiana State University Health Sciences Center, Lions Club, and Research to Prevent Blindness.

CONFLICT OF INTERESTS

The author has no conflicts of interest to declare.

REFERENCES

1 Linsenmeier RA, Braun RD, McRipley MA, Padnick LB, Ahmed J, Hatchell DL, McLeod DS, Lutty GA. Retinal hypoxia in long-term diabetic cats. Invest Ophthalmol Vis Sci. 1998 Aug;39(9):1647-57. PubMed PMID: 9699554.

2. Wangsa-Wirawan ND, Linsenmeier RA. Retinal oxygen: fundamental and clinical aspects. Arch Ophthalmol. 2003 Apr;121(4):547-57. Review. PubMed PMID: 12695252.

3. Lau JC, Linsenmeier RA. Increased Intraretinal PO2 in Short-Term Diabetic Rats. Diabetes. 2014 Dec;63(12):4338-42. doi: 10.2337/db14-0101. Epub 2014 Jul 15. PubMed PMID: 25028524.

4. Riva CE, Pournaras CJ, Tsacopoulos M. Regulation of local oxygen tension and blood flow in the inner retina during hyperoxia. J Appl Physiol (1985). 1986 Aug;61(2):592-8. PubMed PMID: 3745049.

5. Cranstoun SD, Riva CE, Munoz JL, Pournaras CJ. Continuous measurements of intra-vascular pO2 in the pig optic nerve head. Klin Monbl Augenheilkd. 1997 May;210(5):313-5. PubMed PMID: 9230497.

6. Riva CE. Noninvasive measurement of oxygen tension in the optic nerve head. Curr Opin Ophthalmol. 1998 Apr;9(2):56-60. Review. PubMed PMID: 10180515.

7. Shahidi M, Wanek J, Blair NP, Little DM, Wu T. Retinal tissue oxygen tension imaging in the rat. Invest Ophthalmol Vis Sci. 2010 Sep;51(9):4766-70. doi: 10.1167/iovs.09-4710. Epub 2010 Apr 7. PubMed PMID: 20375336.

8. Khoobehi B, Beach JM, Kawano H. Hyperspectral imaging for measurement of oxygen saturation in the optic nerve head. Invest Ophthalmol Vis Sci. 2004 May;45(5):1464-72. PubMed PMID: 15111603.

9. Beach J, Ning J, Khoobehi B. Oxygen saturation in optic nerve head structures by hyperspectral image analysis. Curr Eye Res. 2007 Feb;32(2):161-70. PubMed PMID: 17364749.

10. Gorman A, Fletcher-Holmes DW, Harvey AR. Generalization of the Lyot filter and its application to snapshot spectral imaging. Opt Express. 2010 Mar 15;18(6):5602-8. doi: 10.1364/OE.18.005602. PubMed PMID: 20389576.

11. Hardeberg JY, Schmitt F, Brettel H. Multispectral color image capture using a liquid crystal tunable filter. Opt. Eng. 41(10), 2532–2548 (2002).

12. Harvey AR, Fletcher-Holmes DW. Birefringent Fourier-transform imaging spectrometer. Opt. Express 12(22), 5368–5374 (2004).

13. Harvey AR, Beale JE, Greenaway AH, Hanlon TJ, Williams JW.

Technology options for hyperspectral imaging. Proc. SPIE 4132, 13–24 (2000).
14. Weitzel L, Krabbe A, Kroker H, Thatte N, Tacconi-Garman LE, Cameron M, Genzel R, Tacconi Garman LE. 3D: The next generation near-infrared imaging spectrometer. Astron. Astrophys. Suppl. Ser. 119(3), 531–546 (1996).
15. Fletcher-Holmes DW, Harvey AR. Spectral imaging with a hyperspectral fovea. J. Opt. A, Pure Appl. Opt. 7(6), S298–S302 (2005).
16. Descour MR, Volin CE, Dereniak EL, Thome KJ, Schumacher AB, Wilson DW, Maker PD. Demonstration of a high-speed nonscanning imaging spectrometer. Opt. Lett. 22(16), 1271–1273 (1997).
17. Johnson WR, Wilson DW, Fink W, Humayun M, Bearman G. Snapshot Hyperspectral Imaging in Ophthalmology. J. Biomed. Opt. 12(1), 014036 (2007).
18. Wagadarikar AA, Pitsianis NP, Sun X, Brady DJ. Video rate spectral imaging using a coded aperture snapshot spectral imager. Opt. Express 17(8), 6368–6388 (2009).
19. Beach JM, Schwenzer KJ, Srinivas S, Kim D, Tiedeman JS. Oximetry of retinal vessels by dualwavelength imaging: calibration and influence of pigmentation. J Appl Physiol. 1999;86:748–758.
20. Hammer M, Vilser W, Riemer T, Schweitzer D. Retinal vessel oximetry-calibration, compensation for vessel diameter and fundus pigmentation, and reproducibility. J Biomed Opt. 2008;13: 54015.
21. Tiedeman JS, Kirk SE, Srinivas S, Beach JM. Retinal oxygen consumption during hyperglycemia in patients with diabetes without retinopathy. Ophthalmol. 1998:105:31–36.
22. Hardarson S, Stefansson E. Oxygen saturation in branch retinal vein occlusion. Acta Ophthalmol. 2012;90:466–470.
23. Hammer M, Vilser W, Riemer T, et al. Diabetic patients with retinopathy show increased retinal venous oxygen saturation. Graefes Arch Clin Exp Ophthalmol. 2009;247:1025–1030.
24. Hardarson S, Stefansson E. Retinal oxygen saturation is altered in diabetic retinopathy. Br J Ophthalmol. 2012;96:560–563.
25. Khoobehi B, Firn K, Thompson H, Reinoso M, Beach J. Retinal arterial and venous oxygen saturation is altered in diabetic patients. Invest Ophthalmol Vis Sci. 2013 Oct 29;54(10):7103-6. doi: 10.1167/iovs.13-12723. PubMed PMID: 24114546.
26. Schweitzer D, Hammer M, Kraft J, Thamm E, Konigsdorffer E, Strobel J. *In vivo* measurement of the oxygen saturation of retinal vessels in healthy volunteers. IEEE Trans Biomed Eng. 1999;12:1454–1465.
27. Schweitzer D, Thamm E, Hammer M, Kraft J. A new method for the measurement of oxygen saturation at the human ocular fundus. Int Ophthalmol. 2001;23:347–353.
28. Hammer M, Roggan A, Schweitzer D, Müller G. Optical properties of ocular fundus tissues-an *In vitro* study using the double-integrating-sphere technique and inverse Monte Carlo simulation. Phys Med Biol. 1995;40:963–978.
29. Hammer M, Schweitzer D. Quantitative reflection spectroscopy at the human ocular fundus. Phys Med Biol. 2002;47:179–191.
30. Hammer M, Thamm E, Schweitzer D. A simple algorithm for *In vivo* ocular fundus oximetry compensating for non-haemoglobin absorption and scattering. Phys Med Biol 2002;47:N233-N238. PMID: 12361226
31. Tiedeman JS, Kirk SE, Srinivas S, Beach JM. Retinal oxygen consumption during hyperglycemia in patients with diabetes without retinopathy. Ophthamology 105: 31-36,1998.
32. Harris A, Kageman L, Amin C, Migliardi R, Ciulla T, Arend O. A New Spectrographic Digital Fundus Oxymeter: Effect of Hyperoxia on Retinal Oxygen Tension. DOG-Jubilaumstagung 2002 Sept.
33. Crittin M, Schmidt H, Riva CE. Hemoglobin oxygen saturation (So2) in the human ocular fundus measured by reflectance oximetry: preliminary data in retinal veins. Klin Monatsbl Augenheilkd 2002 Apr;219(4):289-91.
34. Burgansky-Eliash Z, Nelson DA, Bar-Tal OP, Lowenstein A, Grinvald A, Barak A. Reduced retinal blood flow velocity in diabetic retinopathy. Retina. 2010 May;30(5):765-73. PubMed PMID: 20061994.
35. Geirsdottir A, Palsson O, Hardarson SH, et al. Retinal vessel oxygen saturation in healthy individuals. Ophthalmol. Vis. Sci. 53: 5433-5442 (2009).
36. Hammer M, Riemer T, Vilser W, et al. A new imaging technique for retinal vessel oximetry: principles and first clinical results in patients with retinal arterial occlusion and diabetic retinopathy. Proc. SPIE 7163: 1-3 (2000).
37. Hardarson SH, Gottfredsdottir MS, Halldorsson GH, et al. Glaucoma filtration surgery and retinal oxygen saturation. Invest. Ophthalmol. Vis. Sci. 50(11): 5247-5250 (2009).

Peer reviewer: Qianying Gao, Zhongshan Ophthalmic Center, Sun Yat-sen University, 54 S. Xianlie Road Guangzhou 510060 People's Republie of China.